



High performance hydrogen production of MoS₂-modified perovskite LaNiO₃ under visible light

Min Mao¹ · Jing Xu^{1,2,3} · Lingjiao Li¹ · Sheng Zhao¹ · Xuanhao Li¹ · Yanru Li¹ · Zeying Liu¹

Received: 29 April 2019 / Revised: 17 July 2019 / Accepted: 9 August 2019 / Published online: 29 August 2019
© Springer-Verlag GmbH Germany, part of Springer Nature 2019

Abstract

A novel composite perovskite LaNiO₃ photocatalyst modified by MoS₂ was synthesized by sol-high temperature calcination. When the molar ratio of La/Ni was 2:1, MoS₂ accounts for 3% of the MoS₂/LaNiO₃ composite catalyst. The hydrogen production activity is up to 47.1 μmol h⁻¹. In the visible range (≥ 420 nm), the hydrogen generation of the composite photocatalyst is increased more than three times that of pure LaNiO₃. It is described that the hydrogen production capacity of catalytic materials formed by MoS₂-modified LaNiO₃ is significantly improved under visible light, the electron and hole pairs are effectively separated, the electron transfer rate is increased, and the recombination of electron and hole pairs is reduced. Furthermore, the experimental results were measured by energy spectrum (XPS), X-ray diffraction (XRD), photoluminescence spectroscopy (PL), scanning electron microscope (SEM), UV–Vis transmission electron microscopy (TEM), and electrochemical workstation. This is consistent with the hydrogen production capacity of the catalyst.

Keywords LaNiO₃ · MoS₂ · Photocatalytic · Hydrogen production · Perovskite

Introduction

The environmental pollution problem caused by the era of large-scale industrialization brought about by economic growth is imminent, and the search for green and efficient catalysts has become a key issue of concern to the world [1, 2]. As an efficient and safe energy source, hydrogen, which exhibits a high calorific value (39.4 kW h⁻¹ kg⁻¹) among all energy materials and does not produce any secondary damages during production, is a key target of many researchers in recent years [3]. In addition to solar energy as a natural, inexhaustible source of green energy, photocatalytic hydrogen production is the key to solving today's world energy problems.

The preparation of photocatalytic materials, the novelty of catalysts, and catalytic performance are the top priorities of sustainable chemical development.

Semiconductor materials have better light-receiving activity, and the generation and transfer efficiency of photo-generated charges are high, which has led to some research on semiconductor catalytic materials. Photocatalytic materials such as BiOOH/g-C₃N₄ [4], MoS₂/CdS [5, 6], RGO-Cu₂O/Fe₂O₃ [7], MoS₂/g-C₃N₄ [8], and g-C₃N₄/GRO/MoS₂ [9] have good catalytic properties. However, there are also defects such as severe preparation conditions and low efficiency of photogenerated electron excitation. In order to find a novel and efficient catalytic material, further exploration and research are needed.

Binary metal oxides have special physicochemical properties and a variety of crystal structures, conforming to the chemical formula of ABO₃ form, called perovskite, which is a promising new matrix in the field of photocatalysis [10]. The two metal elements are related to the crystallinity of the catalyst and the performance structure such as electron defects [11]. By controlling these parameters, the catalytic activity of the semiconductor photocatalyst is improved. In recent years, the hierarchical structure of perovskites has been initially studied, such as CaTiO₃ and ATaO₃ (A = Li, Na, K). [12, 13]. All showing good photocatalytic activity. However, the

✉ Jing Xu
wgyxj2000@163.com

¹ School of Chemistry and Chemical Engineering, North Minzu University, Yinchuan 750021, People's Republic of China

² Key Laboratory of Chemical Engineering and Technology (North Minzu University), State Ethnic Affairs Commission, Yinchuan 750021, People's Republic of China

³ Ningxia Key Laboratory of Solar Chemical Conversion Technology Autonomous Region, North Minzu University, Yinchuan 750021, People's Republic of China

catalyst for the replacement of the A-site metal in the perovskite by rare-earth ions has not received sufficient attention, and the reports on the effects of properties and structures are also limited. However, the rare earth perovskite catalyst has defects such as weak response to light and large forbidden bandwidth. Therefore, it is key to explore this paper to find a catalyst to modify rare-earth perovskite materials and to supplement defects to improve photocatalytic performance.

Transition metal sulfides have become the focus due to their excellent electrical and optical properties [14]. The good two-dimensional nanostructure structural type of MoS_2 makes the electron acceptability strong and cost low, and is regarded as the best substitute for metal Pt [6, 15, 16]. The poor conductivity of molybdenum disulfide itself is the main reason for the weak catalytic performance of the monomer [8, 9], but the high catalytic performance of the composite catalyst formed by combining it with other catalytic materials is not to be underestimated. The specificity of the electronic structure of rare earth elements has unparalleled spectral characteristics [17]. When the substance is excited by light, the light-induced electrons promote the reduction reaction, and the generated holes induce oxidation reaction, which is the beginning of the photocatalytic process [11]. La is widely used in the preparation of photocatalysts [18]. The extremely high electron accepting power of MoS_2 combines with the excellent spectral characteristics of rare earths to inhibit the reverse generation of electrons and holes, improving the hydrogen evolution ability of substances through effective transfer of electrons.

In this paper, the process of synthesizing $\text{MoS}_2/\text{LaNiO}_3$ composite photocatalyst by sol-high temperature calcination method is introduced, exploring the hydrogen evolution ability of the catalyst in the visible range of the sensitizing system (eosin EY). The chemical interaction of $\text{MoS}_2/\text{LaNiO}_3$ composite catalyst formed on the surface of LaNiO_3 is relatively stable. By optimizing the ratio (molar) of La/Ni and the mass ratio of $\text{MoS}_2/\text{LaNiO}_3$, the composite photocatalyst of $\text{MoS}_2/\text{LaNiO}_3$ has high catalytic activity under the irradiation of 300 W Xe lamp. The H_2 release ability of the composite photocatalyst formed by MoS addition significantly increases the activity of pure LaNiO_3 , which is about 3 times, and the photocurrent density, the response intensity to light, and the recombination rate of photogenerated electrons are superior to those of pure LaNiO_3 . The photocatalyst has remarkable long-term stability for the production of H_2 . Based on the photochemical and resolved photoluminescence measurements, the mechanism of catalyst hydrogen evolution reaction is speculated. The reason for improving the performance can be attributed to the high charge separation efficiency and light utilization efficiency of the incident light.

Experimental section

The chemicals used are analytical reagents and can be used without further purification. Lanthanum nitrate ($\text{La}(\text{NO}_3)_3 \cdot 6\text{H}_2\text{O}$), nickel nitrate ($\text{Ni}(\text{NO}_3)_2 \cdot 6\text{H}_2\text{O}$), ammonium heptamolybdate tetrahydrate ($(\text{NH}_4)_6\text{Mo}_7\text{O}_{24} \cdot 4\text{H}_2\text{O}$), and thiourea ($\text{CH}_4\text{N}_2\text{S}$) were all purchased from Aladdin. This study also used Sodium hydroxide (NaOH), hexadecyl trimethyl ammonium bromide (CTAB), and sodium dodecyl benzene sulfonate (SDBS). Deionized water is used in all experiments.

Preparation of LaNiO_3 and $\text{MoS}_2/\text{LaNiO}_3$

In the preparation of LaNiO_3 , the CTAB of 0.01 mol and the SDBS of 0.02 mol (the molar ratio is 1:2) were stirred and dissolved in deionized water at 30 °C for 18 h to obtain the vesicle solution. $\text{La}(\text{NO}_3)_3 \cdot 6\text{H}_2\text{O}$ and 0.217 g $\text{Ni}(\text{NO}_3)_2 \cdot 6\text{H}_2\text{O}$ (n (La): n (Ni) = 3: 1, 2: 1, 1: 1, and 1:2 respectively recorded as LaNiO_3^{-1} , LaNiO_3^{-2} , LaNiO_3^{-3} , LaNiO_3^{-4}) were dissolved in a vesicle liquid prepared above 75 ml. The precipitate was obtained by dropping the NaOH solution with 0.1 mol/L until the pH value of the solution reached 8.5. Generate a cyan precipitate for filtration, washed to remove the anionic contained therein. The precipitates were dried at 70 °C for 10 h, ground evenly with agate mortar, then fired 5 h at 750 °C in a muffle furnace, and heated at the rate of 5 °C min^{-1} , to prepare LaNiO_3 . In the 200 mg LaNiO_3 prepared above, the corresponding mass $(\text{NH}_4)_6\text{Mo}_7\text{O}_{24} \cdot 4\text{H}_2\text{O}$ and $\text{CH}_4\text{N}_2\text{S}$ (so that the mass ratio of the formed MoS_2 to $\text{MoS}_2/\text{LaNiO}_3$ is 1%, 2%, 3%, 4%, and 5%, respectively) are dissolved in the deionized water of 60 ml and stirred for 60 min. The precursor was moved to a polytetrafluoroethylene reactor, in an electrothermal thermostatic drying chamber at 180 °C for 16 h and naturally cooled. The product was washed with deionized water to remove the superfluous substance, and the product was dried in a drying box at 70 °C for 5 h.

Research on sample characterization

In the case of Cu $K\alpha$ radiation of 40 kV and 40 mA current, the crystallographic peaks in the range of 10° to 80° were recorded by X-ray diffraction (XRD) to investigate the crystal structure and constituent materials of the material. At an accelerating voltage of 5 kV, the morphology of the sample was measured by field emission scanning electron microscopy (SEM). Further exploration of the morphology and composition of the sample was done with the help of JEOL JEM-2100 200kV instrument field transmission electron microscopy (TEM) and high-resolution projection (HRTEM). The elemental

composition and elemental chemical state of the catalytic sample were investigated by conventional X-ray photoelectron spectroscopy (XPS) under ultra-high vacuum VG ESCALAB 250 electron spectrometer. At room temperature, the photoluminescence spectrum (PL) of the sample was explored under a FLUOROMAX-4 spectrophotometer. The degree of response of the sample to visible light (UV-visDRS) was measured under a UV-2550 (Shimadzu) spectrometer. The BET data of the sample records the specific surface area and pore size of the catalyst, which was explored at 77 K using the ASAP 2020 M instrument.

Photocatalytic hydrogen evolution experiments

The photocatalytic reaction was studied by 300 W Xe light with 420-nm cutoff filter under the rotator. The hydrogen evolution test of the catalyst was carried out in a 250-ml quartz vessel with the aid of a magnetic stirrer. The specific operation is to uniformly mix 20 mg of catalyst and 100 ml of triethanolamine (TEOA, 10%) solution (electron sacrificial agent) and place it in an ultrasonic instrument for 20 min. Adjusting the pH of TEOA with 10% TEOA, 0.1 mol·L⁻¹ HCl solution, or 10% 0.1 mol·L⁻¹ NaOH solution, 50 mg eosin (EY) was suspended in the above solution as a sensitizing agent and stirred in a magnetic stirrer for 30 min. We add nitrogen to the reaction system and remove the oxygen inside with a needle for 40 min. Under visible light, 0.5 ml H₂ was extracted every 60 min. The amount of hydrogen evolution of the sample was determined with the aid of gas chromatography with SP-2100, 13X column, TCD, and N₂ as the carrier. Under the same experimental conditions, the quantum efficiency of the hydrogen production of the catalyst measured by a bandpass filter through which monochromatic light at different wavelengths (420 nm, 450 nm, 475 nm, 500 nm, 520 nm, and 550 nm) was passed. The photon flux of the incident light at different wavelengths is detected by an optical power meter (CEL-NP2000, 190 nm–11,000 nm, 0–2000 mw/cm⁻²). Quantum efficiency (AQE) is obtained using the following formula:

$$AQE = \frac{2 \times \text{the number of evolved hydrogen molecules}}{\text{the number of incident photon}} \times 100\%$$

Determination of photoelectrochemical characterization

Conductive glass (ITO) was washed and soaked in dilute NaOH, dilute HCl, and anhydrous ethanol solution, and dried

in air. The catalyst (12 mg) was added to a 5-ml ethanol solution, dispersed in an ultrasonic apparatus, and at room temperature evaporated to a viscous liquid. The viscous liquid is then applied to the surface of the conductive glass electrode ITO by a pipette and dried under the natural wind. In a 0.2 M Na₂SO₄ support solution, the reference electrode is a saturated calomel electrode (SCE), and the counter electrode is a platinum electrode in a standard three-electrode cell, placed under the conditions provided by an electrochemical analyzer (Chenhuachi 660E) explored. The immersion area of the conductive working electrode in the support solution is about 0.98 cm². The visible light excitation ultraviolet light is filtered under the condition that the cut filter (420 nm) is provided by a 300 W xenon lamp. The photocurrent response and the volt-ampere characteristic of the sample are placed under a photodiode with an on and off cycle.

Results and discussion

SEM analysis

The morphology of the catalyst is an aspect verification of the catalytic performance of the sample. The surface morphology of each catalyst was studied by emission scanning electron microscopy (SEM). The consequences were shown in Fig. 1. As seen in Fig. 1a, the micromorphology of the LaNiO₃ sample which looks like popcorn, about 2.5 μm in size, indicates that there are many active sites. It can be seen in Fig. 1b that MoS₂ is a flower-like shape composed of nanosheets and the size of a single nanosheet is about 500 nm. Figure 1c shows the morphology of MoS₂/LaNiO₃ composite catalyst with 3% MoS₂. Drawn from it, the single nanosheet on the surface of LaNiO₃ bulk material indicated that the two substances are successfully combined. This structural increases the surface area of the composite catalyst, had more adsorption sites, which promotes the hydrogen evolution ability of the catalyst.

TEM

The morphology of the photocatalyst is an important parameter related to product performance. Figure 2 shows a typical transmission electron micrograph of the prepared sample. It can be seen that the sample consists of a large piece and a monolithic substance loaded on it, where in the dark part of the image is the multilayer nanosheet structure of MoS₂, so that the particle structure becomes irregular [19]. The size of the particles is about 500 nm. Figure 2b is a HRTEM image of the sample, where the images show different lattice fringes; the lattice stripe pitch are 0.23 nm and 0.27 nm, respectively, representing the (103) crystal plane of MoS₂ and the (110)

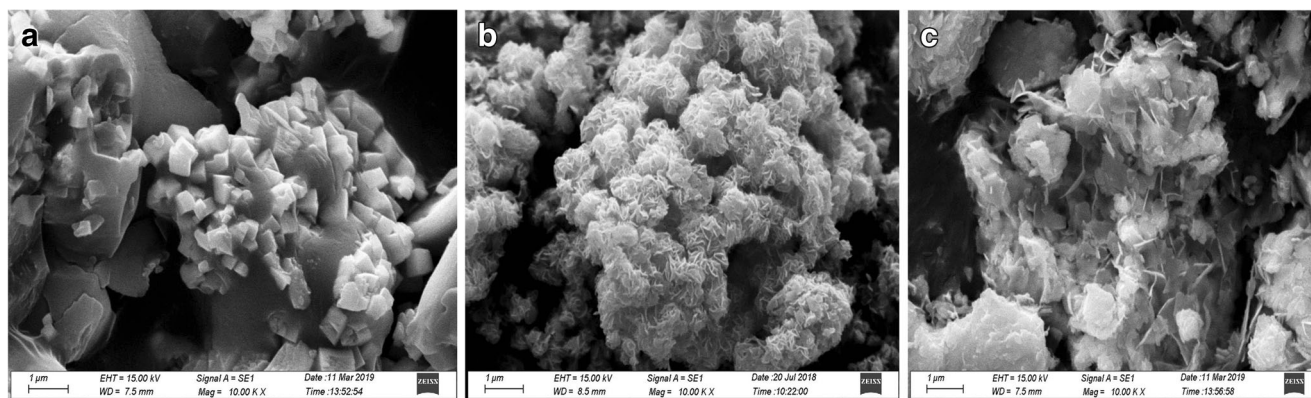


Fig. 1 a SEM images of LaNiO_3 . b MoS_2 samples. c $\text{MoS}_2/\text{LaNiO}_3$ samples

crystal plane of LaNiO_3 , indicating that the composite of MoS_2 and LaNiO_3 is successfully synthesized. Figure 2 c is a general map of the elemental mapping of the

sample. Images from Fig. 2d–h show La, Ni, O, Mo, and S elements in the catalyst, respectively, corresponding to the above scanning discussion.

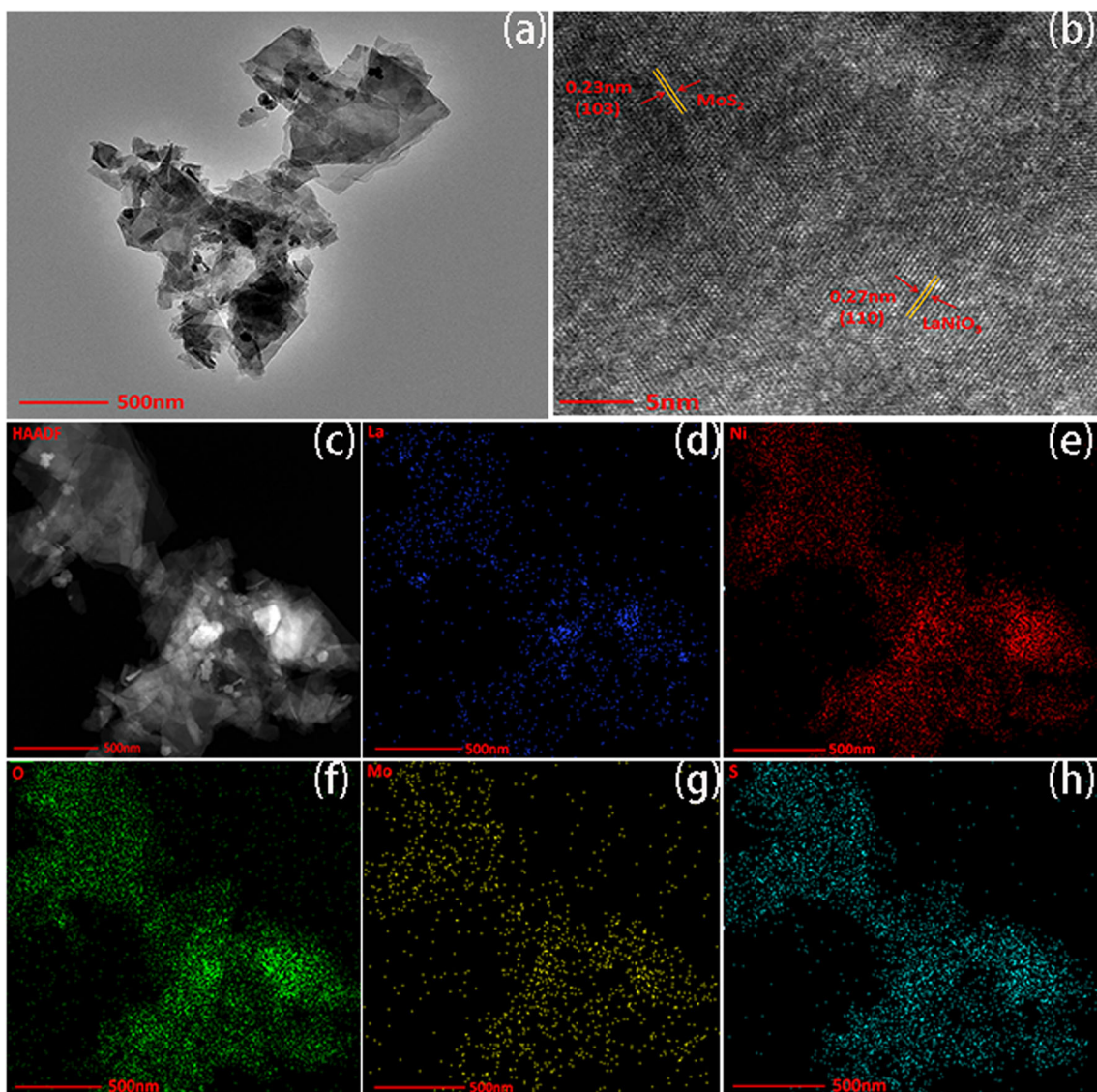


Fig. 2 a The TEM pattern of $\text{MoS}_2/\text{LaNiO}_3$. b The HRTEM pattern of $\text{MoS}_2/\text{LaNiO}_3$. c The mapping master pattern of $\text{MoS}_2/\text{LaNiO}_3$. d, e, f, g, h The mapping element pattern of Mo, S, La, Ni, and O

XRD analysis

As seen in Fig. 2a, the XRD graphics of LaNiO_3 shows several obvious diffraction peaks at $2\theta = 23.32^\circ, 32.89^\circ, 47.36^\circ, 58.68^\circ, 68.88^\circ, 69.76^\circ, 78.69^\circ, \text{ and } 79.08^\circ$ respectively. The diffraction peak can correspond to the crystal plane of LaNiO_3 (JCPDF No.34-1028) characteristic diffraction peak (101), (110), (202), (122), (220), (024), (312), and (214). The XRD spectra of MoS_2 show several obvious characteristic peaks at 2θ that were $14.38^\circ, 33.51^\circ, 39.54^\circ, \text{ and } 58.33^\circ$, which were compared with the characteristic diffraction peaks of MoS_2 (JCPDF No.37-1492) (002), (101), (103), and (110) crystal planes which correspond to each other. This indicates that LaNiO_3 and MoS_2 material was successfully synthesized. Line C in Fig. 2a shows the peaks of $\text{MoS}_2/\text{LaNiO}_3$. The line not only exhibits the characteristic peaks of MoS_2 , but also shows the characteristic peaks of LaNiO_3 , and shows strong and sharp diffraction peaks in similar positions. Figure 2b is an expanded XRD spectrum of 2θ in Fig. 2a, ranging from 31° to 37° . Drawn from it, the strongest characteristic peaks of MoS_2 and LaNiO_3 are 32.89° and 33.51° , respectively. Compared with the pure materials, the 2θ angle of the XRD peak of $\text{MoS}_2/\text{LaNiO}_3$ is slightly shifted due to the complex of the two substances, which indicates that the two substances have been well combined together, $\text{MoS}_2/\text{LaNiO}_3$ substance was successfully synthesized, the peak and the strong peak indicate that the crystallinity of the sample is high [20]. In addition, we have not detected any peaks from and other impurities.

XPS analysis

XPS diagram is an important measure to detect the chemical environment and the content of elements on the surface of the

catalyst. The XPS scanning spectra of $\text{MoS}_2/\text{LaNiO}_3$ composite catalyst are shown in Fig. 3a. It is clear that La, Ni, O, S, and Mo elements are present in the composite catalyst. In the La3d region of Fig. 3b, the peak of $\text{La}3d_{3/2}$ is at 851.86 and 855.45 eV, and the peak of $\text{La}3d_{5/2}$ is at 838.42 and 834.87 eV. These peaks correspond to the La^{3+} of $\text{MoS}_2/\text{LaNiO}_3$ [21]. Figure 3c shows the XPS map of Ni2p. The strongest Ni2p_{3/2} peak of the composite catalyst is about 854.7 eV, while the Ni2p_{1/2} peak is about 871.9 eV. In the oxidizing environment, two characteristic peaks of Ni^{2+} ions and Ni^{3+} ions correspond to them [22]. The peaks at 861.2 eV and 879.0 eV are satellite peaks of Ni2p_{3/2} and Ni2p_{1/2}. Due to the alternating condition of $\text{Ni}^{3+} \leftrightarrow \text{Ni}^{2+}$ in the perovskite material LaNiO_3 , the increase of Ni^{3+} ions brings about the appearance of satellite peak at 861.2 eV, indirectly proving the successful synthesis of the substance LaNiO_3 [23]. In addition, the XPS spectrum appears at 531.25 eV in the region of O1s (Fig. 3d), which can be attributed to the O^{2-} in $\text{MoS}_2/\text{LaNiO}_3$. As shown in Fig. 3e, the peaks of Mo3d are located at 228.96 eV ($\text{Mo}3d_{5/2}$) and 232.36 eV ($\text{Mo}3d_{3/2}$), which are in good agreement with the reported values [24]. It is confirmed that Mo^{4+} is the main oxidation state of MoS_2 [25]. Figure 3f shows the two peaks of 161.87 eV and 162.6 eV, which are S2p_{3/2} and S2p_{1/2} in MoS_2 [26], indicating that S^{2-} is the major valence of substance MoS_2 . XPS results show that the participation of positive valences La, Ni, and Mo metal state and negative valences S and O provides a basis for the formation of $\text{MoS}_2/\text{LaNiO}_3$ and LaNiO_3 [27].

Photocatalytic hydrogen evolution activity of $\text{MoS}_2/\text{LaNiO}_3$ photocatalytic

Adjusting the molar ratio of La to Ni to optimize the catalytic ability of LaNiO_3 single substance, the adjusted ratios of the

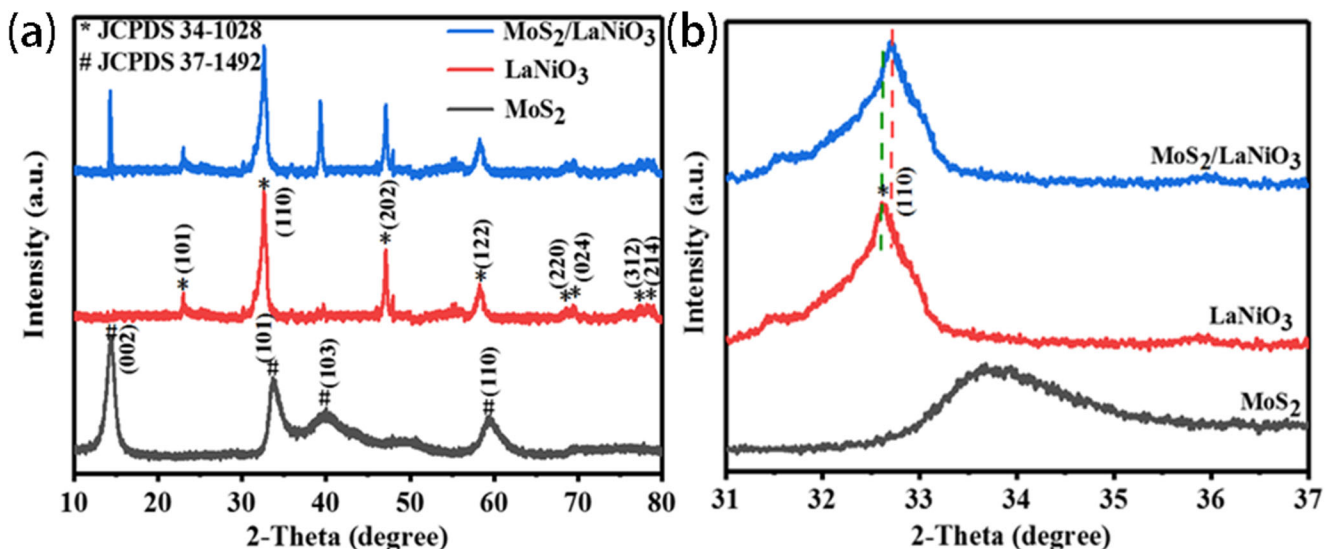


Fig. 3 a XRD patterns of MoS_2 , LaNiO_3 , and $\text{MoS}_2/\text{LaNiO}_3$. b Magnification of diagram a between 31 and 37 degrees

two were 3:1, 2:1, 1:1, and 1:2, respectively. Figure 4 a illustrates the activity of the catalytic material. As the molar ratio of the two elements decreases, the activity of photocatalyst rises first and then decreases. When the molar ratio of the two elements is 2:1, the hydrogen evolution performance reaches its maximum value, and the cumulative hydrogen yield in 5 h is 70.89 μmol . On the basis of the optimum ratio, other factors affecting the photocatalyst were explored.

The results are obtained from Fig. 4b; the EY-sensitized $\text{MoS}_2/\text{LaNiO}_3$ (MoS_2 content mass ratios are 1%, 2%, 3%, 4%, and 5%) is exposed to visible light ($\lambda \geq 420 \text{ nm}$). The hydrogen production of pure LaNiO_3 catalyst can only reach 70.89 μmol after exposure to visible light for 5 h, which indicates that the hydrogen production ability of LaNiO_3 catalyst under illumination response is low, and the separation efficiency of LaNiO_3 catalyst from photogenerated electron hole may be limited. The low efficiency of electron transport is related to the combination of photocharge, which means that only a small amount of electrons escape to the surface of the catalyst, and the binding rate of H^+ and electrons in the reaction solution is very low, thus the hydrogen production is small. When metal sulfide MoS_2 was added into LaNiO_3 to prepare $\text{MoS}_2/\text{LaNiO}_3$ photocatalyst, the catalytic ability of the sample was obviously improved under the equivalent reaction situation. The mass ratio of MoS_2 to LaNiO_3 was adjusted to 1%, 2%, 3%, 4%, and 5%, the hydrogen productions for 5 h were 130.32, 147.1, 235.48, 160.34, and 137.45 μmol , respectively. It is concluded that the catalytic performance of

the composition is best when the mass ratio of MoS_2 is 3% and reached more than three times than that of the pure LaNiO_3 . One reason is that LaNiO_3 is a large structure, which provides lots of adhesion space for MoS_2 ; moreover, the addition of MoS_2 can promote the separation of LaNiO_3 electron holes and increase electron transfer rate, so that the hydrogen production performance of the composites is improved. However, an increase in the number of MoS_2 accumulates on LaNiO_3 , and excess molybdenum masked the active sites of LaNiO_3 . From the optimization exploration of composite samples, it is shown that metal sulfide (MoS_2) has greatly improved the activity of LaNiO_3 to produce hydrogen.

As shown in Fig. 4c, when adjusting the pH value of TEOA is different, the proton concentration in the solution will change and the hydrogen production capacity of the composite sample has obvious changes. The redox potential of photocatalyst and the adhesion between the sensitizing dye and the catalytic sample are also disturbed [28]. The pH value of 10% TEOA solution was adjusted with 0.1 mol/L HCl and 0.1 mol/L NaOH solution, and the hydrogen production efficiency of the catalyst under different pH conditions was determined. Figure 4 c shows the changing trend of the catalytic activity of the catalyst for hydrogen production. Adjusting the pH of an electronic sacrificial agent between 8 and 12, as the alkalinity of the electronic sacrificial agent increases, the catalytic ability changes significantly. It can be seen that when the pH was 10, the catalytic ability of the sample reached the highest, and the catalytic ability reached 235.48 μmol , after

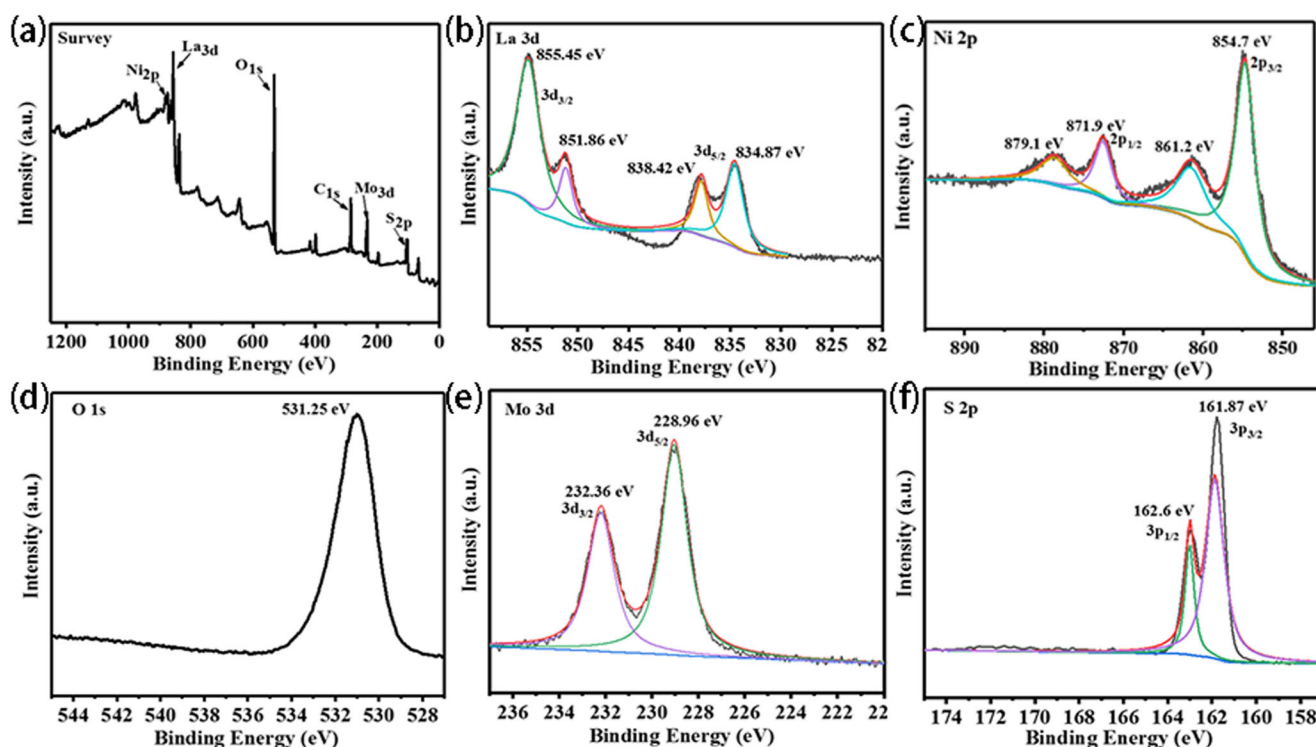


Fig. 4 XPS patterns of $\text{MoS}_2/\text{LaNiO}_3$ sample. a Survey spectra. b La 3d. c Ni 2p. d O 1s. e Mo 3d. f S 2p

the reaction time was 5 h. The reason may be that when the basicity of the electron sacrificial agent is 10, the proton concentration in the solution is most favorable for the adhesion of the dye on the sample, and the hydrogen production can be increased. However, when the solution alkalinity is biased to neutral, the process of H^+ formation of H_2 is inhibited.

In order to explore the interaction between EY and the catalyst, the hydrogen evolution ability of the hydrogen production system at different dosages of blush was explored. As shown in Fig. 5d, with the increase in the amount of eosin, the amount of hydrogen evolution first increased and then decreased. When the dosage was 50 mg, the effect was the best. When the dosage is 40 and 50 mg, the hydrogen evolution ability is small. When the amount of EY is 55 and 60 mg, the hydrogen evolution value of the system is not good. This may be due to the fact that the excess of EY will mask the active site of the catalyst, resulting in a decrease in the sensitizing ability and photogenerated charge. When the EY itself absorbs a large number of light sources, it will be quenched, causing light loss and the dye will also fail. Therefore, EY can provide the catalyst with the advantage of bringing electrons in the system, and the unsuitable dosage will bring disadvantages to the system.

Figure 6 e is a comparison of hydrogen production performance between each single catalyst and different composite catalysts. It can be clearly seen that there are significant differences in the hydrogen evolution capacities of different combinations of catalysts in the same hydrogen production system. It can be seen that pure EY does not have the ability to produce

hydrogen, and the hydrogen evolution of pure MoS_2 and $LaNiO_3$ is also relatively low. When EY and the two single catalysts are respectively combined, the catalytic performance is obviously improved, because EY is only a sensitizing dye, it has a strong adsorption capacity and can generate photoelectrons under the induction of light to provide the catalyst and further promote the hydrogen production of the catalyst. It is concluded from the figure that when the two single catalysts are combined, the hydrogen production capacity is better than that of the single catalyst, indicating that there is also a certain interaction between the two single catalysts, thereby promoting the performance of the catalyst (there is a specific analysis in the following hydrogen production mechanism section). When EY and the composite catalyst are combined, the hydrogen production capacity of the system is optimized, thereby showing a good coordination effect between the components.

Figure 5 f shows the quantum efficiency of the composite catalyst. It can be seen that under different wavelength cutoff filters, the catalyst has a certain hydrogen production performance, indicating that the photoexcitability of the catalyst is good, and the catalyst has an excitation wavelength of 475 nm. The quantum efficiency is optimal (3.68%), and the overall data demonstrates that the photocatalytic ability of the catalyst is good.

In order to determine the stability of the catalyst, the continuous hydrogen production reaction of the catalyst and the XRD and XPS of the used catalyst were studied, and the results are shown in Fig. 6. Figure 6 a shows the stability test, after the end of one cycle of hydrogen production, the reaction

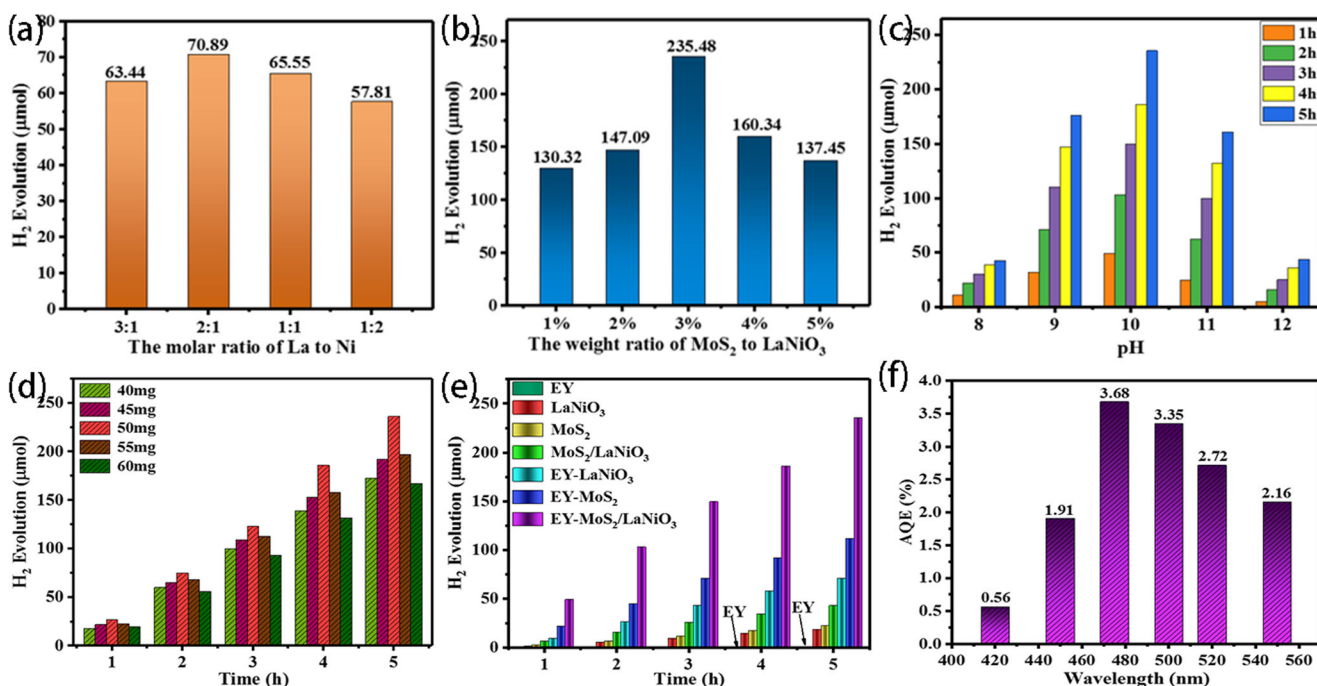


Fig. 5 a Photocatalytic activities for H_2 production with different mole ratios of La/Ni photocatalytic. b Photocatalytic activities for H_2 production with different mole ratios of $MoS_2/LaNiO_3$ photocatalytic. c Effect of different pH on photocatalytic activity of $MoS_2/LaNiO_3$ system. d

Hydrogen production changes in different blush dosages (40–60 mg). e Comparison chart of hydrogen production performance of different catalysts. f AQE of 3% $MoS_2/LaNiO_3$ under different wavelengths from 400 to 600 nm

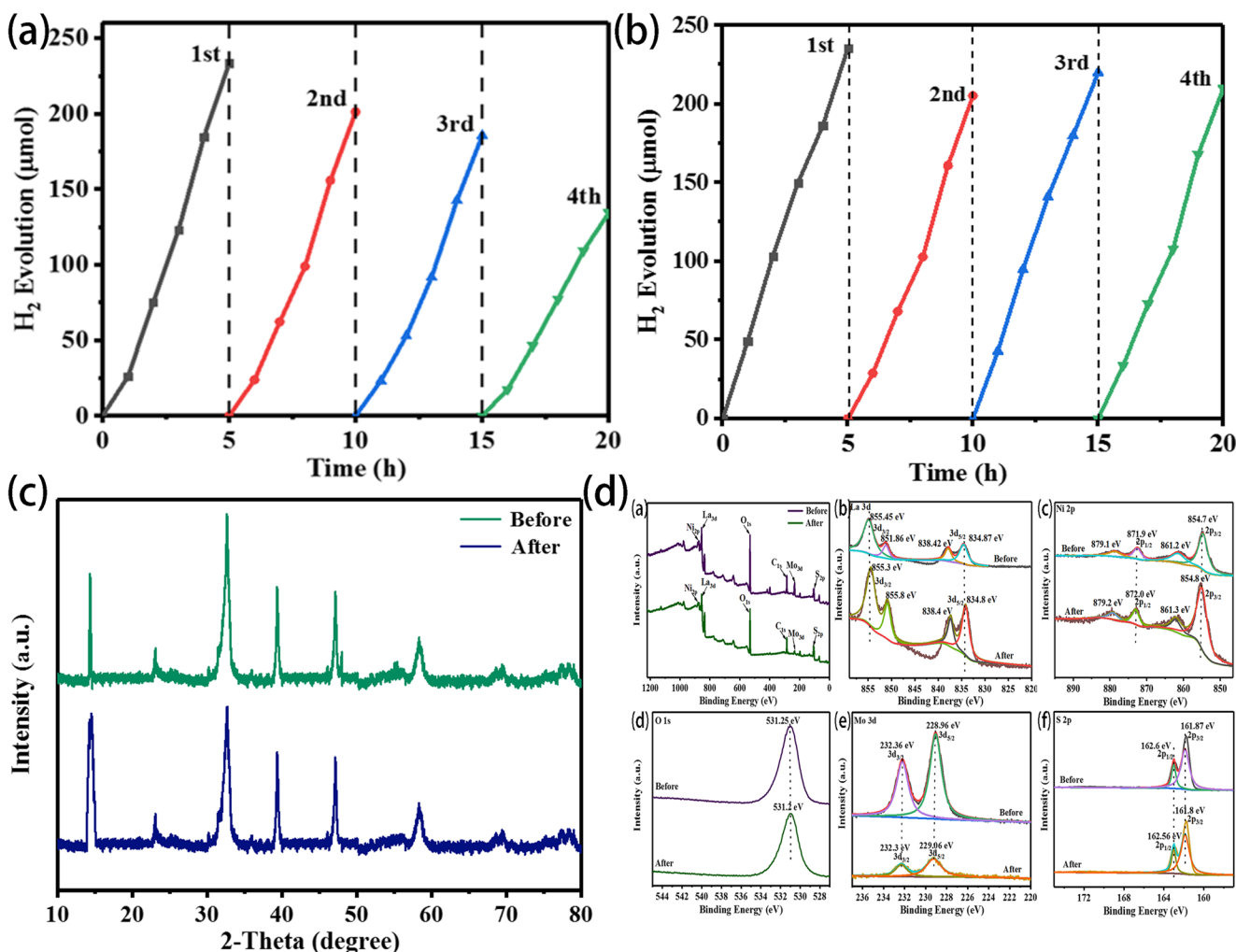


Fig. 6 a, b Hydrogen production cycle diagram of 3% MoS₂/LaNiO₃. c XRD pattern of the 3% MoS₂/LaNiO₃ after the reaction. d XPS pattern of the 3% MoS₂/LaNiO₃ after the reaction

gas in the hydrogen bottle is completely replaced with nitrogen and no substance is added, and then the subsequent cycle of hydrogen production is continued. It can be seen that the hydrogen production efficiency of the second, third, and fourth cycles is gradually reduced. The second, third, and fourth cycle hydrogen production rates were 91.75%, 68.75%, and 55.56% for the first time respectively. The cyclic test operation of Fig. 6b is different from that of Fig. 6a. Before the start of the third cycle, an appropriate amount of EY is added to the system, resulting in an increase in hydrogen evolution capacity, the second and fourth times were lower than the first and second. By comparison, it is found that EY dye is a key factor affecting the amount of hydrogen evolution in the system, because EY dye has poor stability, easy to desorb, easy to diffuse in solution, and easy to degrade under illumination. Therefore, dye molecules severely limit the catalytic performance of the sample [29]. From the perspective of the whole cycle, the catalytic ability of the sample is relatively stable, which indirectly indicates that the stability of the sample is good. In order to further prove the stability of the

catalyst, the XRD and XPS spectra of the used catalyst are shown in Fig. 6c and d, and there is no significant change in the characteristic peak compared with the spectrum before the reaction, indicating that the catalyst has good stability.

Photo-luminescence (PL) analysis

To further verify the performance of the catalyst, capture, transition, and annihilation efficiency of photogenerated electrons have been measured by photoluminescence spectroscopy. The rate of photogenerated charge transfer is related to the peak height of the fluorescent peak, and the height of the peak indicates the rate at which electrons and holes combine. Figure 7 shows the induced fluorescence intensity of EY, EY-LaNiO₃, EY-MoS₂, and EY-MoS₂/LaNiO₃ aqueous solution at an excitation wavelength of 480 nm. As the picture shows, the fluorescence intensities of EY, EY-LaNiO₃, EY-MoS₂, and EY-MoS₂/LaNiO₃ show the main peaks with different intensities at about wavelength of 538 nm. The pure EY solution has the highest fluorescence peak, with the

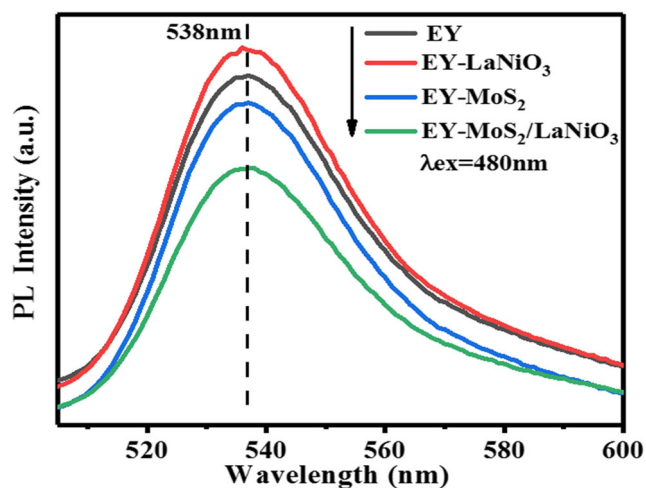


Fig. 7 Fluorescence spectra of EY-sensitized (1×10^{-6} mol L⁻¹) MoS₂, LaNiO₃, and MoS₂/LaNiO₃ in 10% TEOA aqueous solution at pH = 10

introduction of LaNiO₃ and MoS₂, the fluorescence peak gradually decreases, indicating that there is a significant interaction between EY and LaNiO₃ and EY and MoS₂. The electrons generated by EY under illumination are transferred to MoS₂ and LaNiO₃, thereby increasing the fluorescence quenching rate [30]. The luminescence intensity of EY-MoS₂/LaNiO₃ is the weakest, indicating that the photoelectrons generated by LaNiO₃ are effectively transferred to MoS₂ under illumination, and the synergy between the three effectively reduces the quenching of fluorescence, prevents the binding of hole electrons of LaNiO₃, and thus reduces the emission peak intensity of fluorescence, which is consistent with the effect of photocatalytic hydrogen production [31].

To deeply explore the quenching principle of LaNiO₃ fluorescence by MoS₂ and the effect of MoS₂ on photocharge transfer of LaNiO₃, time-resolved fluorescence measurements were also demonstrated. As a function of time, the transient fluorescence of the sample was measured. As shown in Table 1, the single exponential fluorescence decay kinetics can describe the fluorescence attenuation of single substance EY, indicating that there is a fluorescent substance in the electronic sacrificial agent with a lifetime of 0.163 ns. After the addition of MoS₂, LaNiO₃, and MoS₂/LaNiO₃, the fluorescence decay of EY was characterized by double exponential fluorescence kinetics [32]. The average life expectancy was

0.177 ns, 0.307 ns, and 0.323 ns, respectively. This is because the addition of MoS₂ effectively transfers electrons of LaNiO₃ and at the same time inhibits the recombination of electron holes, thus generating more photoelectrons and increasing the lifetime [33, 34]. It was proved that the photocatalytic hydrogen production activity was significantly improved.

Electrochemical analysis

In order to provide new evidence for studying the transport and separation efficiency of photoexcited carriers, we have measured the transient photocurrent responses of pure LaNiO₃, pure MoS₂ and MoS₂/LaNiO₃ composites under several invisible light irradiation. Figure 8 shows the photocurrent of pure LaNiO₃, pure MoS₂, and MoS₂/LaNiO₃ samples. Obviously, when the light source is introduced and removed, the photocurrent increases and decreases. The photocurrent response of the MoS₂/LaNiO₃ sample increases significantly compared with pure MoS₂ and LaNiO₃ with the role between MoS₂ and LaNiO₃ [35]. The results show that the formation of composite clusters promotes the transfer of surface charge of LaNiO₃, which reduces the recombination of electron holes and promotes the generation of new photoelectrons. This effective coordination between MoS₂ and LaNiO₃ is well reflected in the photocurrent correlation and is the key to improving the catalytic ability.

At the same time, deeper exploration of the hydrogen production capacity of MoS₂/LaNiO₃ is related to the synergism of MoS₂ and LaNiO₃, and LaNiO₃, MoS₂, and MoS₂/LaNiO₃ coated on ITO glass were studied by linear scanning voltammetry (LSV) in the Na₂SO₄ solution of 0.1 mol/L. As shown in Fig. 8b, it can be seen that H⁺ cathode charges on a pure ITO conductive electrode. In the same voltage range, the reduction current density of the blank group, LaNiO₃, MoS₂, and MoS₂/LaNiO₃ electrodes increases gradually [36]. This phenomenon indicates that the synergistic enhancement between MoS₂ and LaNiO₃ is beneficial to the electron transfer of MoS₂/LaNiO₃ photocatalysts. Deeper proofs of the initial reduction potential of empty conductive electrodes, LaNiO₃, MoS₂, and MoS₂/LaNiO₃ electrodes are basically the same, indicating that MoS₂/LaNiO₃ is not only a highly effective photocatalyst. At the same time, it is also a highly active

Table 1 Transient fluorescence lifetime distribution of different samples

Systems ^a	Lifetime, $\langle\tau\rangle$(ns)	Pre-exponential factors A/%	Average lifetime, $\langle\tau\rangle$(ns) ^d	χ^2
EY	= 0.163	A = 100	0.163	1.28
EY-MoS ₂	= 2.896	A ₁ = 6.64	0.177	1.19
	= 0.175	A ₂ = 93.36		
EY-LaNiO ₃	= 0.3	A ₁ = 97.35	0.307	0.983
	= 3.191	A ₂ = 2.63		
EY-MoS ₂ /LaNiO ₃	= 3.81	A ₁ = 2.25	0.323	1.021
	= 0.316	A ₂ = 97.75		

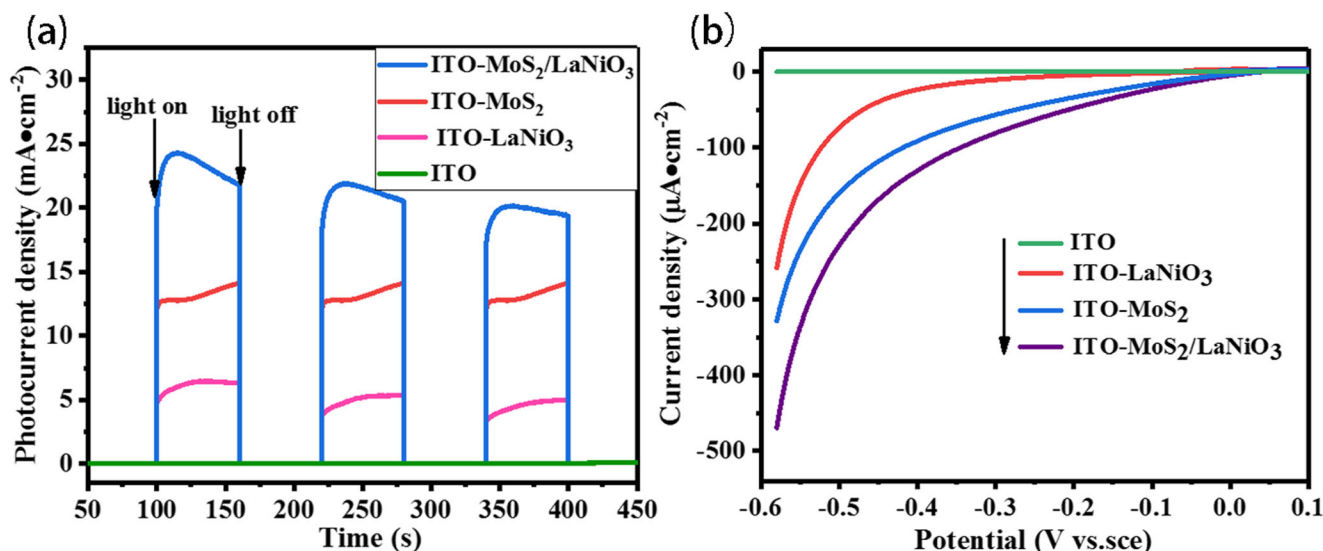


Fig. 8 **a** Photocurrent response under visible light irradiation ($\lambda > 420$ nm). **b** LSV curves of $\text{MoS}_2/\text{LaNiO}_3$, MoS_2 , and LaNiO_3 in Na_2SO_4 (0.2 mol/L). The scan rate was 0.5 mV s^{-1}

electrocatalyst [34]. The existence of MoS_2 can more conducive to photolysis of water and generate hydrogen, which is consistent with the above conclusion.

UV-Vis analysis

The photoresponse behavior of the catalyst and the light absorption characteristics of the catalytic material were further explored by means of UV-Vis spectroscopy (UV-visDRS). Drawn from the graph, a single LaNiO_3 has a strong absorptivity under the light of 200–400 nm. Compared with the single LaNiO_3 , the $\text{MoS}_2/\text{LaNiO}_3$ system shows a slight red shift with the introduction of MoS_2 [37]. MoS_2 and LaNiO_3 have similar photoresponsive abilities in the range of 200–800 nm. Under

the excitation of MoS_2 , the $\text{MoS}_2/\text{LaNiO}_3$ system produces obvious broadband absorption under 300–800 nm of the light. The results show that there is a strong interaction between MoS_2 nanoparticles and LaNiO_3 , which is conducive to the transport and separation of charge carriers [38]. The formula ($\alpha h\nu = A(h\nu - E_g)^n$) is used to calculate the band gap width E_g of these samples. A and $h\nu$ are the light response coefficients and photon energies of different substances, respectively, where A is a fixed amount, $n = 1/2$ or $n = 2$ [39]. As shown in Fig. 9b, the bandgap widths of LaNiO_3 , MoS_2 , and $\text{MoS}_2/\text{LaNiO}_3$ are 2.54 eV, 1.91 eV, and 2.08 eV, respectively. For $\text{MoS}_2/\text{LaNiO}_3$, not only the redshift of the absorption range can be seen, but also a strong absorption range within the wavelength range of 380–800 nm. Compared with pure LaNiO_3 , the light adsorption range of

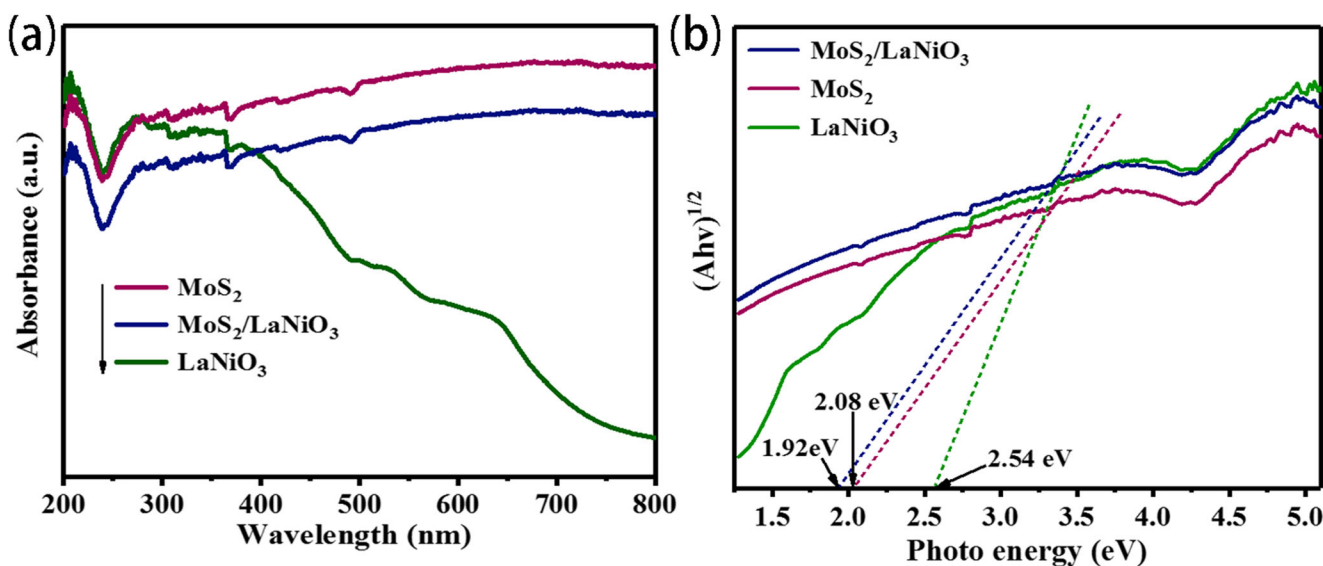


Fig. 9 **a** The UV-Vis diffuse reflectance absorption spectra of MoS_2 , LaNiO_3 , and $\text{MoS}_2/\text{LaNiO}_3$ photocatalysts. **b** Bandgap width map of MoS_2 , LaNiO_3 , and $\text{MoS}_2/\text{LaNiO}_3$ photocatalyst

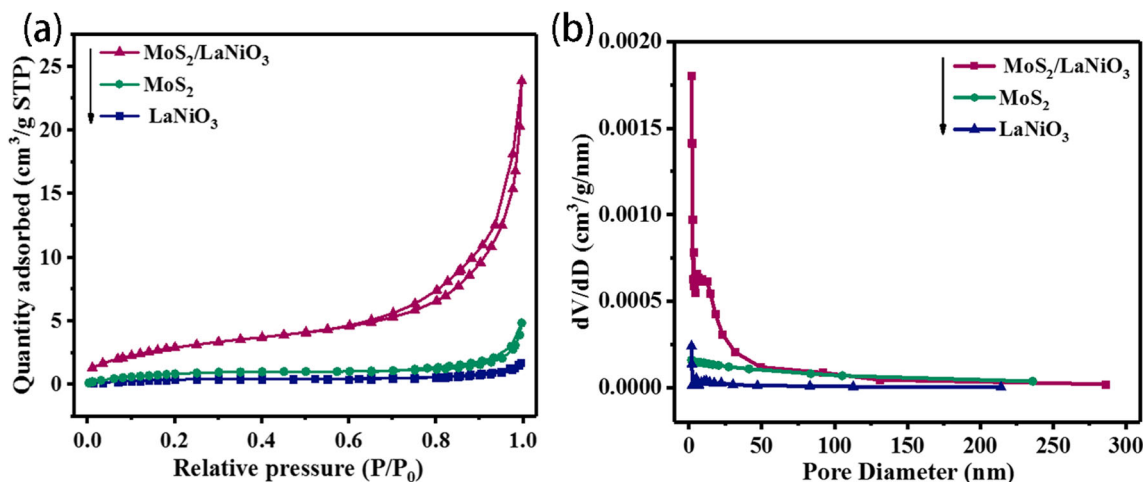


Fig. 10 **a** The N₂ adsorption–desorption isotherms of LaNiO₃, MoS₂, and MoS₂/LaNiO₃. **b** The corresponding pore size distribution curves (insert) of LaNiO₃, MoS₂, and MoS₂/LaNiO₃

MoS₂/LaNiO₃ increases, which means that more visible light can be obtained, which helps to improve the photocatalytic performance [40]. The introduction of MoS₂ has a significant effect on the increase of the light responsiveness of LaNiO₃ and the reduction of the forbidden bandwidth. Such phenomena are the prerequisite for optimizing hydrogen production and also an expression of the interaction between single catalysts.

Brunauer–Emmett–Teller (BET) nitrogen adsorption isotherm characterization

The pore volume and pore size of the sample and the surface area of the particles were determined by a physical adsorb, which was determined by a nitrogen adsorption–desorption method [41]. Figure 10 is a graph showing the pore size distribution and suction and desorption isotherms of different samples. Learning from Fig. 10a, LaNiO₃, MoS₂, and MoS₂/LaNiO₃ are type III isotherms and H₃ hysteresis loops, generated between high pressure ranges between 0.65 and 1 (P/P₀), indicate that the substance has a certain adsorption capacity. As can be seen from Table 2, the specific surface areas of LaNiO₃ and MoS₂ are very small, and strong calcination during the preparation of LaNiO₃ causes the catalyst particles to grow rapidly, resulting in a decrease in specific surface area [42]. With the addition of MoS₂, LaNiO₃ has a significant improvement effect, thus improving the adsorption of the dye in the system and the performance of the composite catalyst, which is the result of the mutual cooperation of the two monomers. The pore sizes of the samples in Table 2 are 16.24 nm, 16.77 nm, and 15.89 nm, respectively, indicating that the catalytic sample is present in the form of mesopores [43]. From the pore size distribution diagram of Fig. 8b, the sample consists of micropores and mesopores, indicating that the addition of MoS₂ changes the structure of the sample, and the La element contained in the catalyst controls the crystal properties of the

sample [44]. The composite sample enhances the capture of sunlight, improved charge transfer, and optimized hydrogen production capacity of the composite catalyst.

The hydrogen production mechanism

Integrating all experiments and characterization results, the mechanism by which the catalyst decomposes hydrogen in water under visible light is presumed. Due to the straddling alignment, heterojunction formed by the interaction between the two monomers promotes the separation and transfer rate of charges, reduces the recombination of electron holes, and improves the hydrogen production ability of the composite. In order to further explain the process of high-efficiency hydrogen production by semiconductor heterojunction, the VB and CB band positions of MoS₂ and LaNiO₃ are estimated by the forbidden bandwidth calculated by UV characterization and the theoretical formula (1) and (2) of Mulliken electronegativity:

$$E_{CB} = \chi - E^e - 0.5E_g \tag{1}$$

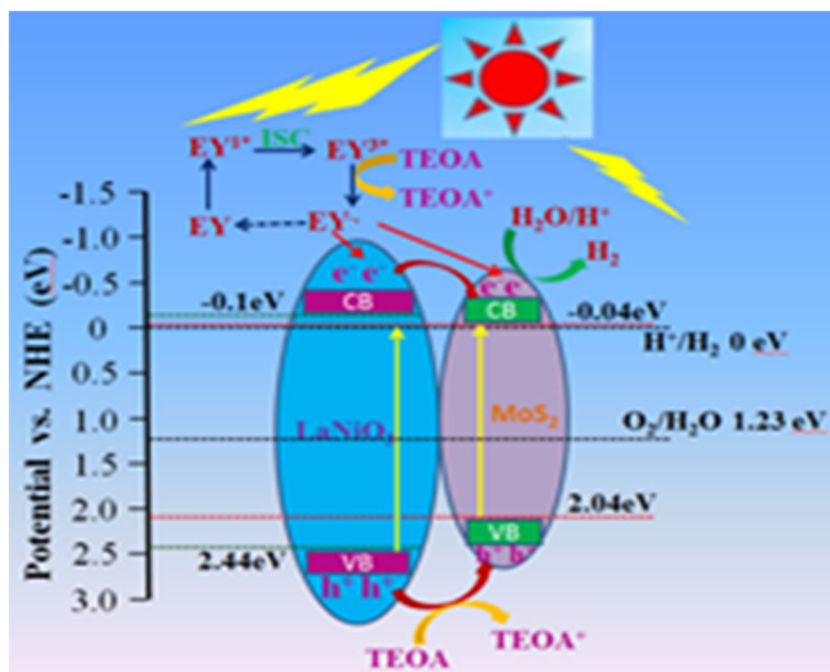
$$E_{VB} = E_{CB} - E_g \tag{2}$$

χ is the geometric mean of the electronegativity of the individual elements constituting the monomer material and becomes absolute electronegativity. The χ of LaNiO₃ and MoS₂ are 5.67 eV and 5.50 eV, respectively

Table 2 The S_{BET}, pore size, and pore volume for LaNiO₃, MoS₂, and MoS₂/LaNiO₃

Samples	S _{BET} (m ² g ⁻¹)	Pore size (nm)	Pore volume (cm ³ g ⁻¹)
LaNiO ₃	1.50	16.24	0.002
MoS ₂	3.33	16.77	0.007
MoS ₂ /LaNiO ₃	10.97	15.89	0.035

Fig. 11 The photocatalytic hydrogen production mechanism over EY-sensitized MoS₂/LaNiO₃ system under visible light irradiation



(see the support information for specific calculations). E° is the energy of free electrons on the hydrogen scale (4.5 eV) [45], and the E_g of LaNiO₃ and MoS₂ are given in Fig. 9b, which are 2.54 eV and 1.92 eV, respectively. Based on the above formula and data, it is concluded that CB and VB of LaNiO₃ are -0.1 eV and 2.44 eV, and CB and VB of MoS₂ are -0.04 eV and 2.04 eV, respectively. Figure 11 illustrates the mechanism of the formation of H₂ over eosin EY sensitized MoS₂/LaNiO₃ photocatalyst. Under the excited by light, EY dye molecules are attached to MoS₂/LaNiO₃ to become a single-weight EY^{1*} excited state, which will transition between systems to become a triplet excited state EY^{3*}. In addition, the electronic sacrificial agent contained in the solution was used as an electron sacrificial agent to quench EY^{3*} to form a reduced dye EY⁻, which forms an oxidized TEOA⁺ [46]. LaNiO₃ and MoS₂ generate photoelectrons and holes under the excitation of light, electrons migrate to the conduction band of the substance, holes are generated in the valence band, and finally, EY⁻ transfers its electrons to the catalyst of LaNiO₃ or MoS₂, the electrons on the LaNiO₃ conduction band are also transferred to the MoS₂ conduction band, and the H⁺ bond in the solution is reduced to H₂, and the holes on the LaNiO₃ valence band migrate toward the valence band of the MoS₂ substance. At the same time, EY⁻ returns to the ground state, and the TEOA is oxidized to TEOA⁺ at the electron hole, and the reaction is completely balanced. This can effectively inhibit the recombination of photogenerated charges, increase charge transfer and generation, and greatly optimize photocatalytic activity.

Conclusions

Non-precious metal LaNiO₃ nanomaterials were successfully synthesized by sol-high temperature calcination, and MoS₂ was further supported on LaNiO₃ to achieve high activity of photocatalytic hydrogen production. From the SEM, TEM, XRD, and XPS diagrams, we can see that the composite catalyst was successfully synthesized, the surface area gets bigger and in favor of charge transfer efficiency. The MoS₂/LaNiO₃ composite photocatalyst has excellent photocatalytic performance in sensitized dye system. Compared with the single LaNiO₃ (70.89 μmol), the hydrogen production of the composite catalyst (235.48 μmol) is more than three times higher than that of the single LaNiO₃. Further studies show that the ratio of La to Ni and the ratio between MoS₂ and LaNiO₃ have an effect on the hydrogen production capacity of the sample. In the LaNiO₃ precursor, the adjusted ratio between La and Ni is 2:1, and when the weight ratio of MoS₂ is 3%, the hydrogen-producing performance of the catalyst is the best. The sample has the best hydrogen production ability when the pH of the electron sacrificial agent is 10. From the fluorescence analysis and electrochemical characterization, the results show that the charge transfer rate on LaNiO₃ was significantly enhanced and the recombination of holes and electrons was decreased by MoS₂ as a compared catalyst. The characterization measures of UV-Vis and BET show that the composite catalyst MoS₂/LaNiO₃ has rich surface area and stronger light response range and smaller band gap, so the composite catalyst is more easily excited. The increase in sample performance is also attributed to the increase in attached dyes. The synergism among LaNiO₃,

MoS₂, and EY dyes improves the activity of the catalyst. The results show that the composite catalyst is an effective catalyst and has a potential application prospect.

Funding information This work was supported by Natural Science Foundation of Ningxia Province (NZ17262).

References

- Wang P, Sihuizhan, Wang H et al (2018) Cobalt phosphide nanowires as efficient co-catalyst for photocatalytic hydrogen evolution over Zn_{0.5}Cd_{0.5}S[J]. *Appl Catal B Environ* 230:210–219
- Purusottam RB, Chandra SM, Poorna PB et al (2018) Photocatalytic, magnetic, and electrochemical properties of La doped BiFeO₃ nanoparticles[J]. *Ceram Int* 44:19512–19521
- Liu D, Jin Z, Li H et al (2017) Modulation of the excited-electron recombination process by introduce g-C₃N₄, on Bi-based bimetallic oxides photocatalyst[J]. *Applied Surface Science* 423:255–265
- Cui Y, Zhang X et al (2019) Construction of BiOCCOOH/g-C₃N₄ composite photocatalyst and its enhanced visible light photocatalytic degradation of amido black 10B[J]. *Sep Purif Technol* 210:125–134
- Zhang J, Zhao Y et al (2019) Density functional theory calculation on facet-dependent photocatalytic activity of MoS₂/CdS heterostructures[J]. *Appl Surf Sci* 469:27–33
- Yong-Jun Y, Zijian L, Shiting W et al (2018) Role of two-dimensional nanointerfaces in enhancing the photocatalytic performance of 2D-2D MoS₂/CdS photocatalysts for H₂ production[J]. *Chem Eng J* 350:335–343
- Shen H, Liu G, Yan X, Jiang J, Hong Y, Yan M, Mao B, Li D, Fan W, Shi W (2017) All-solid-state Z-scheme system of RGO-Cu₂O/Fe₂O₃ for simultaneous hydrogen production and tetracycline degradation [J]. *Mater Today Energy* 5:312–319
- Yong-Jun Y, Zhikai S et al (2019) Liquid exfoliation of g-C₃N₄ nanosheets to construct 2D-2D MoS₂ /g-C₃N₄ photocatalyst for enhanced photocatalytic H₂ production activity [J]. *Appl Catal B Environ* 246:120–128
- Yong-Jun Y, Yan Y et al (2018) Promoting charge separation in g-C₃N₄/graphene/MoS₂ photocatalysts by two-dimensional nanojunction for enhanced photocatalytic H₂ production[J]. *ACS Appl Energy Mater* 1(4):1400–1407
- Gao X, Shang Y, Liu L, Nie W (2019) A plasmonic Z-scheme three-component photocatalyst g-C₃N₄/Ag/LaFeO₃ with enhanced visible-light photocatalytic activities [J]. *Opt Mater* 88:229–237
- Wang R, Ni S, Liu G, Xu X (2018) Hollow CaTiO₃ cubes modified by La/Cr co-doping for efficient photocatalytic hydrogen production[J]. *Appl Catal B Environ* 225:139–147
- Yan Y, Yang H et al (2018) Enhanced photocatalytic activity of surface disorder-engineered CaTiO₃ [J]. *Mater Res Bull* 105:286–290
- Marchena CL, Pecchi GA, Pierella LB (2019) Selective styrene oxidation on alkaline tantalates ATaO₃ (A = Li, Na, K) as heterogeneous catalysts [J]. *Catal Commun* 119:28–32
- Yang Y, Li F, Li W, Gao W, Wen H, Li J, Hu Y, Luo Y, Li R (2017) Porous CoS₂ nanostructures based on ZIF-9 supported on reduced graphene oxide: favourable electrocatalysis for hydrogen evolution reaction[J]. *Int J Hydrog Energy* 42(10):6665–6673
- Yong-Jun Y, Pei W et al (2019) The role of bandgap and interface in enhancing photocatalytic H₂ generation activity of 2D-2D black phosphorus/MoS₂ photocatalyst[J]. *Appl Catal B Environ* 242:1–8
- Zhang S, Zhang G et al (2019) Enhancement of photocatalytic H₂ evolution on pyrene-based polymer promoted by MoS₂ and visible light [J]. *Appl Catal B Environ* 251:102–111
- Pokrant S, Dilger S, Landsmann S, Trottmann M (2017) Size effects of cocatalysts in photoelectrochemical and photocatalytic water splitting [J]. *Mater Today Energy* 5:158–163
- Ao Y, Wang K, Wang P, Wang C, Hou J (2016) Synthesis of novel 2D-2D p-n heterojunction BiOBr/La₂Ti₂O₇ composite photocatalyst with enhanced photocatalytic performance under both UV and visible light irradiation[J]. *Appl Catal B Environ* 194:157–168
- Hua E, Jin S, Wang X, Ni S, Liu G, Xu X (2019) Ultrathin 2D type-II p-n heterojunctions La₂Ti₂O₇/In₂S₃ with efficient charge separations and photocatalytic hydrogen evolution under visible light illumination [J]. *Appl Catal B Environ* 245:733–742
- Alali KT, Liu T, Liu J, Liu Q, Fertassi MA, Li Z, Wang J (2017) Preparation and characterization of ZnO/CoNiO₂, hollow nanofibers by electrospinning method with enhanced gas sensing properties [J]. *J Alloys Compd* 702:20–30
- Xu J, Yu H, Guo H (2018) Synthesis and behaviors of g-C₃N₄, coupled with La_xCo_{3-x}O₄, nanocomposite for improved photocatalytic activity and stability under visible light [J]. *Mater Res Bull* 105:342–348
- Hu J, Cao Y, Xie J, Jia D (2017) Simple solid-state synthesis and improved performance of Ni(OH)₂-TiO₂, nanocomposites for photocatalytic H₂ production[J]. *Ceram Int* 43(14):11109–11115
- Xue Z, Shen Y, Li P, Pan Y, Li J, Feng Z, Zhang Y, Zeng Y, Liu Y, Zhu S (2018) Promoting effects of lanthanum oxide on the NiO/CeO₂, catalyst for hydrogen production by autothermal reforming of ethanol[J]. *Catal Commun* 108:12–16
- Yang X, Huang H, Kubota M, He Z, Kobayashi N, Zhou X, Jin B, Luo J (2016) Synergetic effect of MoS₂ and g-C₃N₄ as cocatalysts for enhanced photocatalytic H₂ production activity of TiO₂[J]. *Mater Res Bull* 76:79–84
- Tang Y, Li X, Zhang D, Pu X, Ge B, Huang Y (2019) Noble metal-free ternary MoS₂/Zn_{0.5}Cd_{0.5}S/g-C₃N₄ heterojunction composite for highly efficient photocatalytic H₂ production[J]. *Mater Res Bull* 110:214–222
- Zhao S, Huang J, Huo Q, Zhou X, Tu W (2016) A non-noble metal MoS₂-Cd_{0.5}Zn_{0.5}S photocatalyst with efficient activity for high H₂ evolution under visible light irradiation[J]. *J Mater Chem A* 4:193–199
- Song W, Ma S, Sun L, Yang Y et al (2017) Urchin-flower like hierarchical LaNiO₃ spheres: structural characteristics and photocatalytic activity[J]. *Chem Technol Ind J* 12:111–120
- Kumar SG, Rao KSRK (2017) Comparison of modification strategies towards enhanced charge carrier separation and photocatalytic degradation activity of metal oxide semiconductors (TiO₂, WO₃ and ZnO) [J]. *Appl Surf Sci* 391:124–148
- Hao X, Jin Z, Yang H, Lu G, Bi Y (2017) Peculiar synergetic effect of MoS₂, quantum dots and graphene on metal-organic frameworks for photocatalytic hydrogen evolution[J]. *Appl Catal B Environ* 210:45–56
- Liu Y, Zhou W, Wang C, Sun L, Wu P (2018) Electronic structure and optical properties of SrTiO₃ codoped by W/Mo on different cationic sites with C/N from hybrid functional calculations[J]. *Comput Mater Sci* 146:150–157
- Huerta-Flores AM, Juárez-Ramírez I, Torres-Martínez LM, Carrera-Crespo JE, Gómez-Bustamante T, Sarabia-Ramos O (2018) Synthesis of AMoO₄, (A=Ca, Sr, Ba) photocatalysts and their potential application for hydrogen evolution and the degradation of tetracycline in water [J]. *J Photochem Photobiol A Chem* 356:29–37
- Yang H, Jin Z, Liu D et al (2018) Visible light harvesting and spatial charge separation over creative Ni/CdS/Co photocatalyst [J]. *J Phys Chem C* 122(19)
- Yang H, Jin Z, Wang G, Liu D, Fan K (2018) Light-assisted synthesis MoS₂ as a noble metal free cocatalyst formed heterojunction CdS/Co₃O₄ photocatalyst for visible light harvesting and spatial charge separation[J]. *Dalton Trans* 47(20):6973–6985

34. Hai Y, Jing X, Zeying L et al (2018) Functionalization of sheet structure MoS₂ with CeO₂-Co₃O₄ for efficient photocatalytic hydrogen evolution[J]. *J Mater Sci* 53(21):15271–15284
35. Li Q, Shi T, Li X, Lv K, Li M, Liu F, Li H, Lei M (2018) Remarkable positive effect of Cd(OH)₂ on CdS semiconductor for visible-light photocatalytic H₂ production[J]. *Appl Catal B Environ* 229:8–14
36. Hai Y, Jing X, Hao G et al (2017) Synergistic effect of rare earth metal Sm oxides and Co_{1-x}S on sheet structure MoS₂ for photocatalytic hydrogen evolution [J]. *RSC Adv* 7(89):56417–56425
37. Yongke Z, Zhiliang J, Hong Y et al (2018) Well-regulated nickel nanoparticles functional modified ZIF-67 (Co) derived Co₃O₄/CdS p-n heterojunction for efficient photocatalytic hydrogen evolution[J]. *Appl Surf Sci* 462:213–225
38. Wu H, Li C, Che H, Hu H, Hu W, Liu C, Ai J, Dong H (2018) Decoration of mesoporous Co₃O₄ nanospheres assembled by monocrystal nanodots on g-C₃N₄, to construct Z-scheme system for improving photocatalytic performance[J]. *Appl Surf Sci* 440:308–319
39. Darsara SA, Seifi M, Askari MB (2018) One-step hydrothermal synthesis of MoS₂/CdS nanocomposite and study of structural, photocatalytic, and optical properties of this nanocomposite[J]. *Optik* 169:249–256
40. Qianqian C, Chunran Z, Yan W et al (2018) Synthesis of MoS₂/YVO₄ composite and its high photocatalytic performance in methyl orange degradation and H₂ evolution[J]. *Sol Energy* 171:426–434
41. Xiaosong Z, Zhihui L, Pingfang T et al (2014) Facile preparation and enhanced photocatalytic H₂ production activity of Cu(OH)₂ nanospheres modified porous g-C₃N₄[J]. *Mater Chem Phys* 143:1462–1468
42. Sun X, Xu X (2017) Efficient photocatalytic hydrogen production over La/Rh co-doped Ruddlesden-Popper compound Sr₂TiO₄ [J]. *Appl Catal B Environ* 210:149–159
43. Dang H, Cheng Z, Yang W, Chen W, Huang W, Li B, Shi Z, Qiu Y, Dong X, Fan H (2017) Room-temperature synthesis of Cu_xS (x=1 or 2) co-modified TiO₂ nanocomposite and its highly efficient photocatalytic H₂ production activity[J]. *J Alloys Compd* 709:422–430
44. Liu Y, Zhou S, Li JM, Wang YJ, Jiang GY, Zhao Z et al (2015) Photocatalytic reduction of CO₂ with water vapor on surface La-modified TiO₂ nanoparticles with enhanced CH₄ selectivity [J]. *Appl Catal B Environ* 168:125–131
45. Li L, Xu J, Ma JP, Liu Z, Li Y (2019) A bimetallic sulfide CuCo₂S₄ with good synergistic effect was constructed to drive high performance photocatalytic hydrogen evolution [J]. *J Colloid Interface Sci* 552:17–26
46. Hao X, Jin Z, Wang F, Xu J, Min S, Yuan H, Lu G (2015) Behavior of borate complex anion on the stabilities and the hydrogen evolutions of Zn_xCo_{3-x}O₄ decorated graphene [J]. *Superlattice Microst* 82:599–611

Publisher's note Springer Nature remains neutral with regard to jurisdictional claims in published maps and institutional affiliations.